Electronic Supplementary Material to An Implementation of Full Cycle Strategy Using Dynamic Blending for Rapid Refresh Short-range Weather Forecasting in China*

Jin FENG[1], Min CHEN[1], Yanjie LI[2], and Jiqin ZHONG[1]

[1]*Institute of Urban Meteorology (IUM)*, *China Meteorological Administration (CMA)*, *Beijing* 100089, *China*

[2]*State Key Laboratory of Numerical Modeling for Atmospheric Sciences and Geophysical Fluid Dynamics*, *Institute of Atmospheric Physics*, *Chinese Academy of Sciences*, *Beijing* 100029, *China*

ESM to: Feng, J., M. Chen, Y. J. Li, and J. Q. Zhong, 2021: An implementation of full cycle strategy using dynamic blending for rapid refresh short-range weather forecasting in China. *Adv. Atmos. Sci.*, **38**(6), 943–956, https://doi.org/10.1007/s00376-021-0316-7.

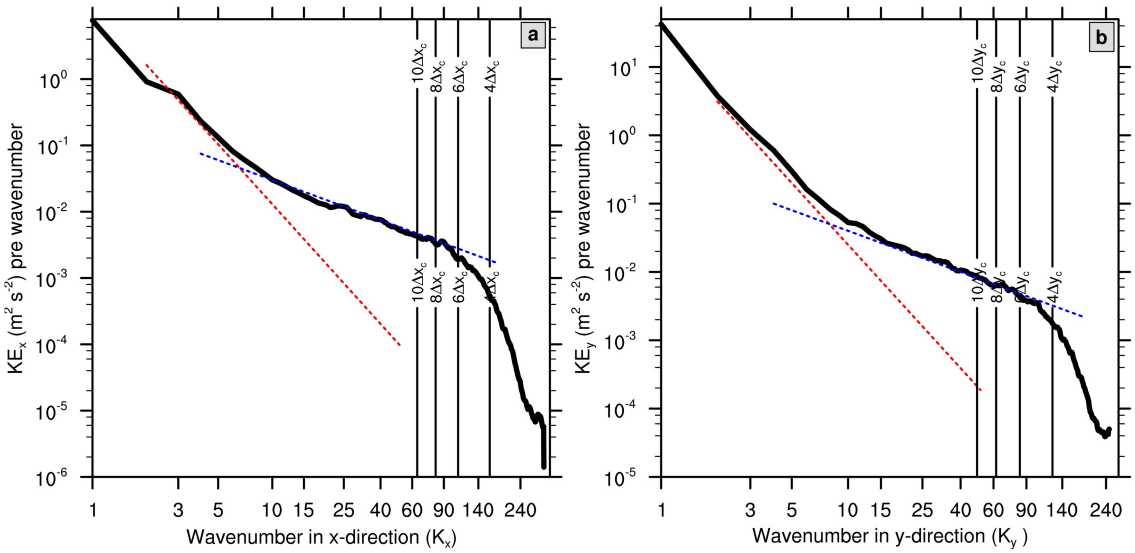

Fig. S1. Time-averaged kinetic energy spectrum from ECMWF data at the 28th model level (~250 hPa) in the (a) *x*- and (b) *y*-directions for the experimental domain in July 2018. The red and blue dotted lines denote the theoretical −3 and −5/3 power-law at the synoptic scale and the mesoscale, respectively. These theoretical power laws were reported by Nastrom and Gage (1985) and Lindborg (1999). The four vertical lines denote the wavenumbers corresponding to 10, 8, 6, and 4 grid spacings in ECMWF. The effective resolution of ECMWF in the experimental domain can be determined by the point at which the model kinetic energy spectra deviate from the theoretical or observed power-law spectra. It should be noted that the original resolution of ECMWF data is about 0.07-degree other than 0.25-degree in released forecast data (see https://confluence.ecmwf.int//display/FCST/Gaussian+grid+with+1280+latitude+lines+between+pole+and+equator).

*The online version of this article can be found at https://doi.org.10.1007/s00376-021-0316-7.

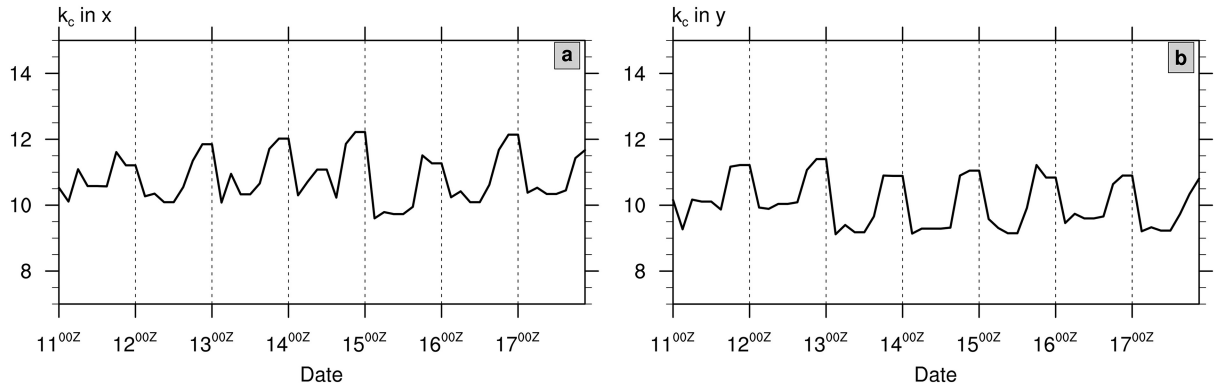

Fig. S2. Temporal variation in the cutoff wavenumber of blending in the (a) *x*- and (c) *y*-directions for experiment FC_DBDA from 0000 UTC 11 July 2018 to 2100 UTC 17 July 2018 (the July cases in section 4). The k_c shows an apparent diurnal oscillation in both *x*- and *y*-directions, with high values from 1800 UTC (0200 Local Standard Time (LST)) to 0000 UTC (0800 LST) but low values from 0300 UTC (1100 LST) to 1200 UTC (2000 LST). More long waves are blended into RMAPS-ST from the ECMWF forecast at nighttime, indicating that DB tends to constrain the large-scale initial field more when the atmospheric state is statically stable. At noon and in the afternoon when the diabatic heating is strong, DB selects a lower cutoff wavenumber to keep more small-scale information from the previous forecast cycle of WRF and to maintain the continuous development of convective systems in the RRC.

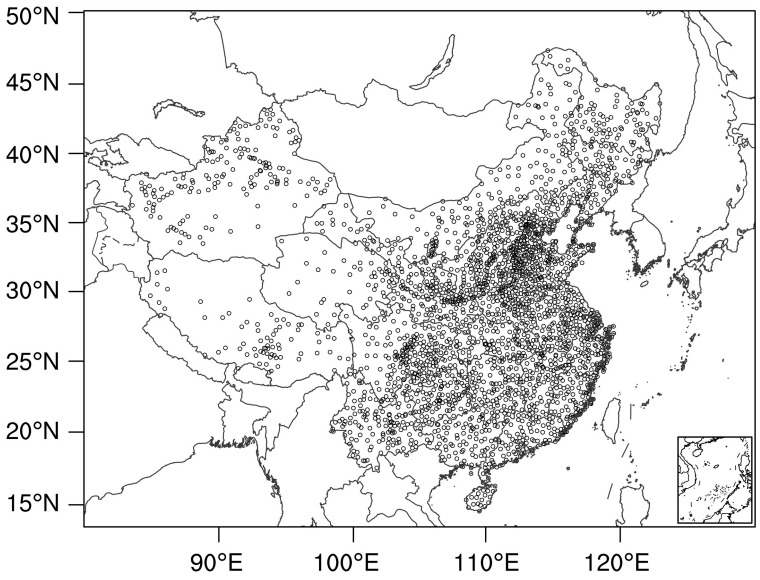

Fig. S3. Geographic distribution of rain gauge sites in China used to verify the precipitation forecasts.

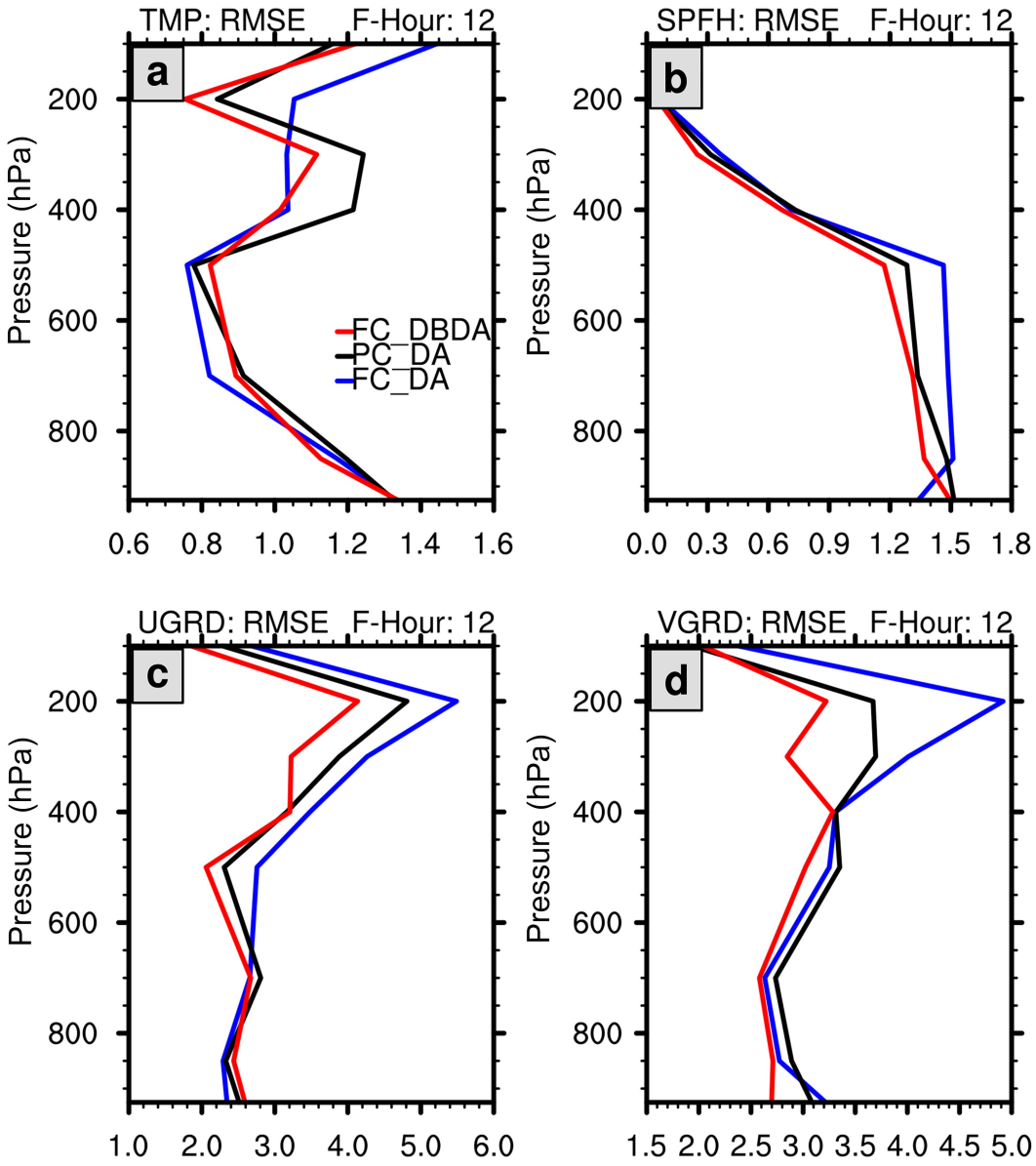

Fig. S4. Same as Fig. 3 but for forecasts at t = 12 h.

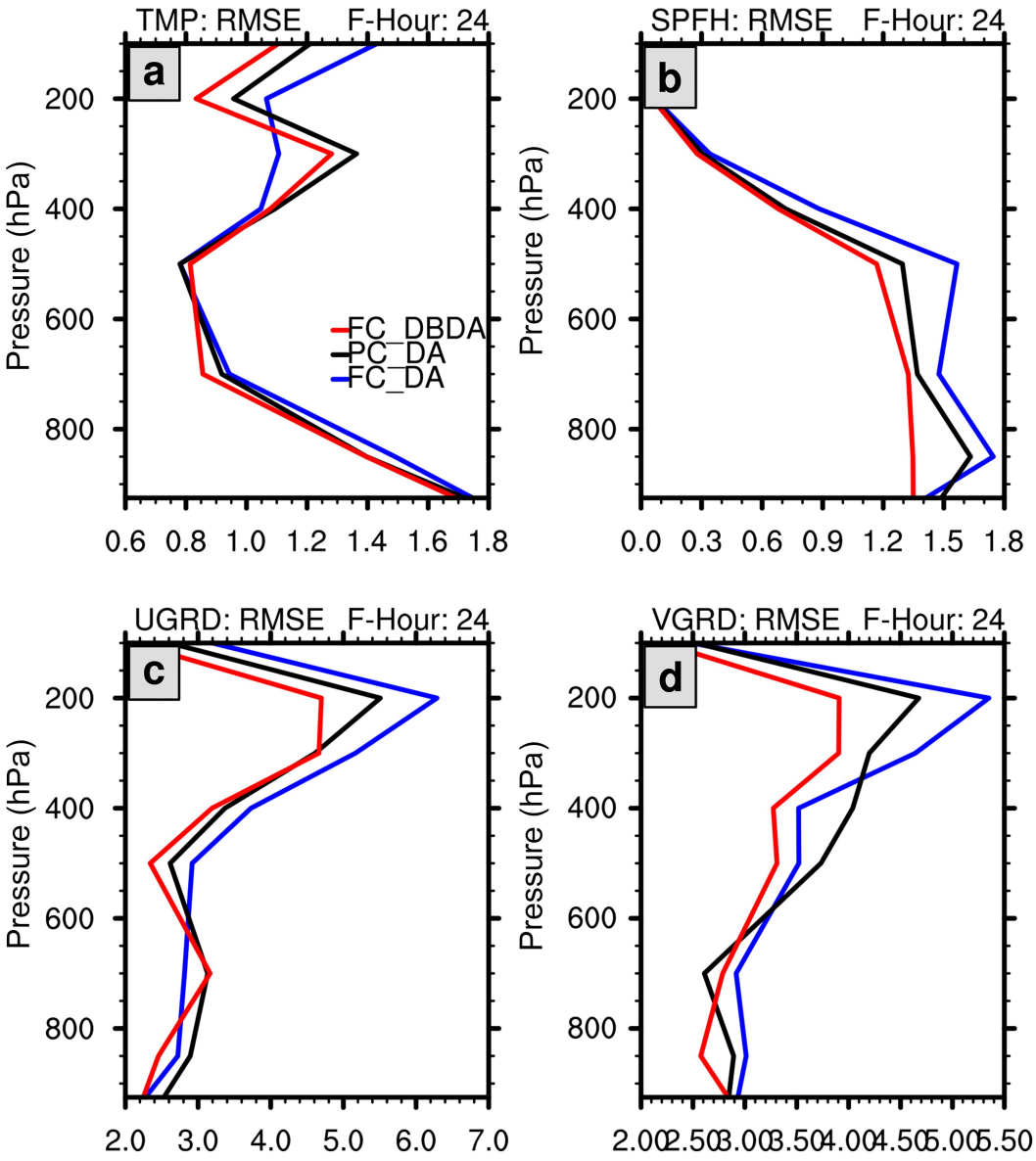

Fig. S5. The same as Fig.3 but for forecasts at t = 24 h.

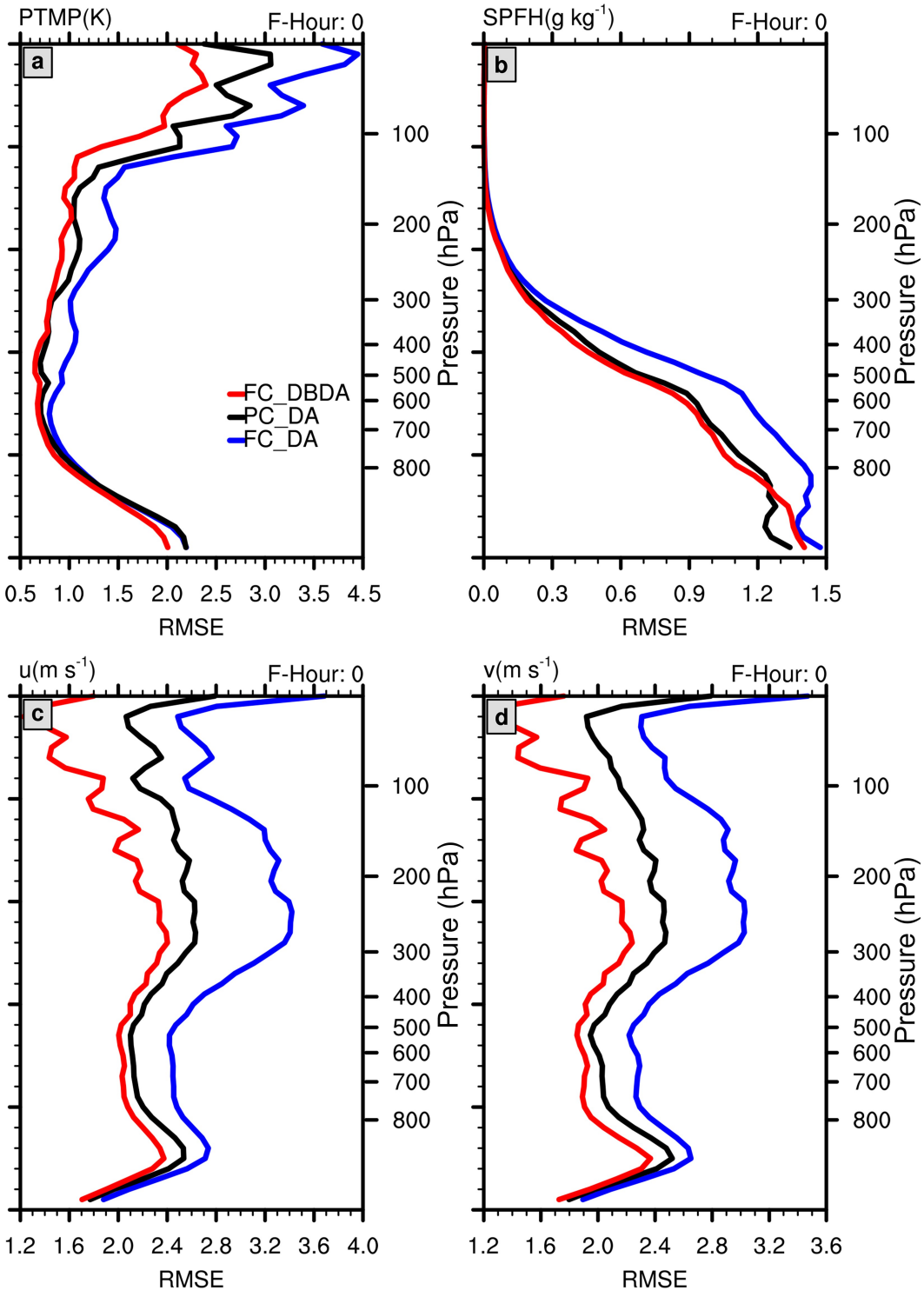

Fig. S6. Multicycle-averaged initial RMSE (t = 0 h) over the experimental domain against GFS final reanalysis data for (a) air temperature (units: K), (b) specific humidity (units: g kg^{-1}), (c) velocity component in x-direction u (units: m s^{-1}), and (d) velocity component in y-direction v (units: m s^{-1}). The black, red and yellow curves denote the RMSEs of FC_DA, PC_DA and FC_DBDA respectively.

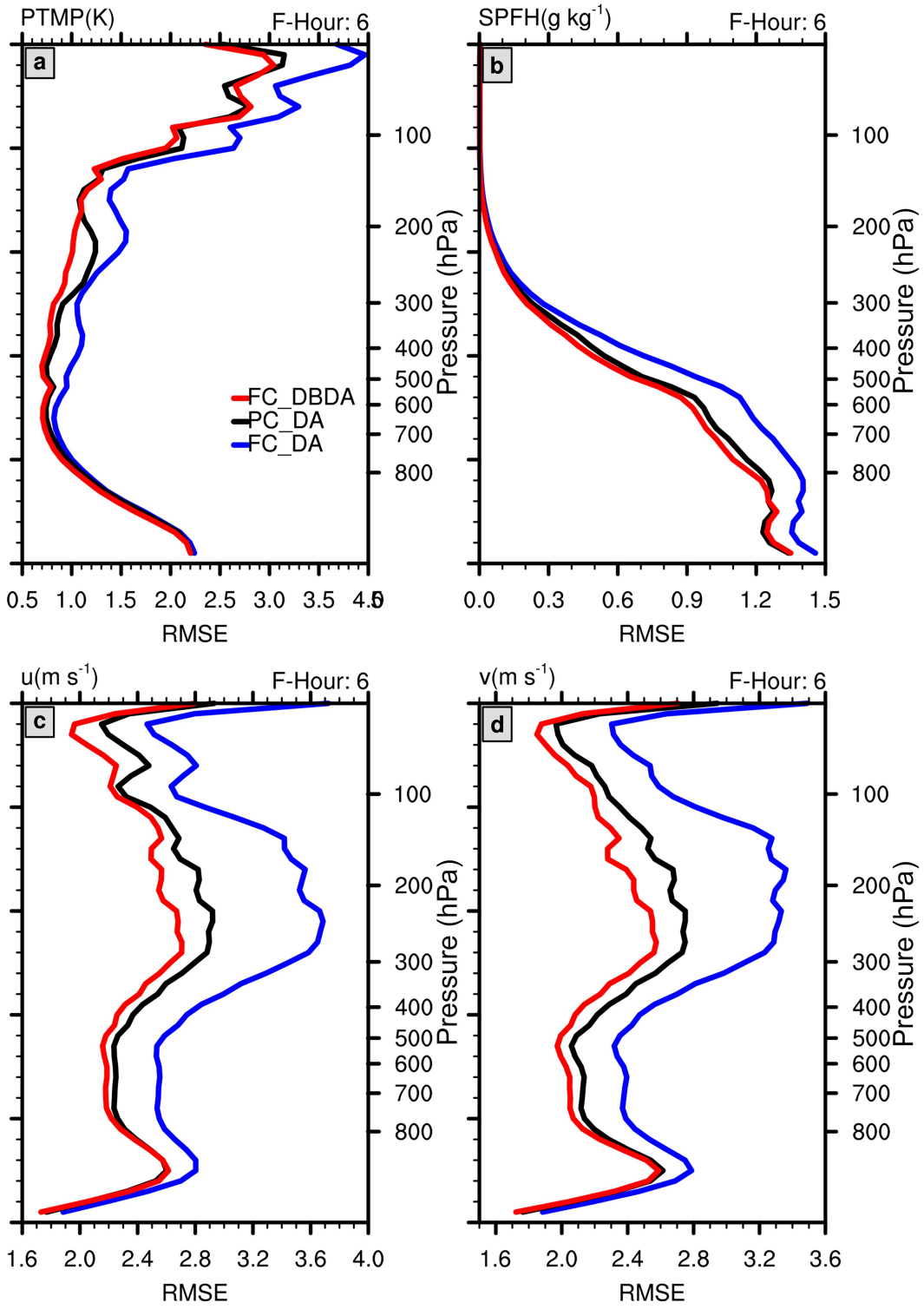

Fig. S7. Same as Fig. S6 but for forecasts at t = 6 h.

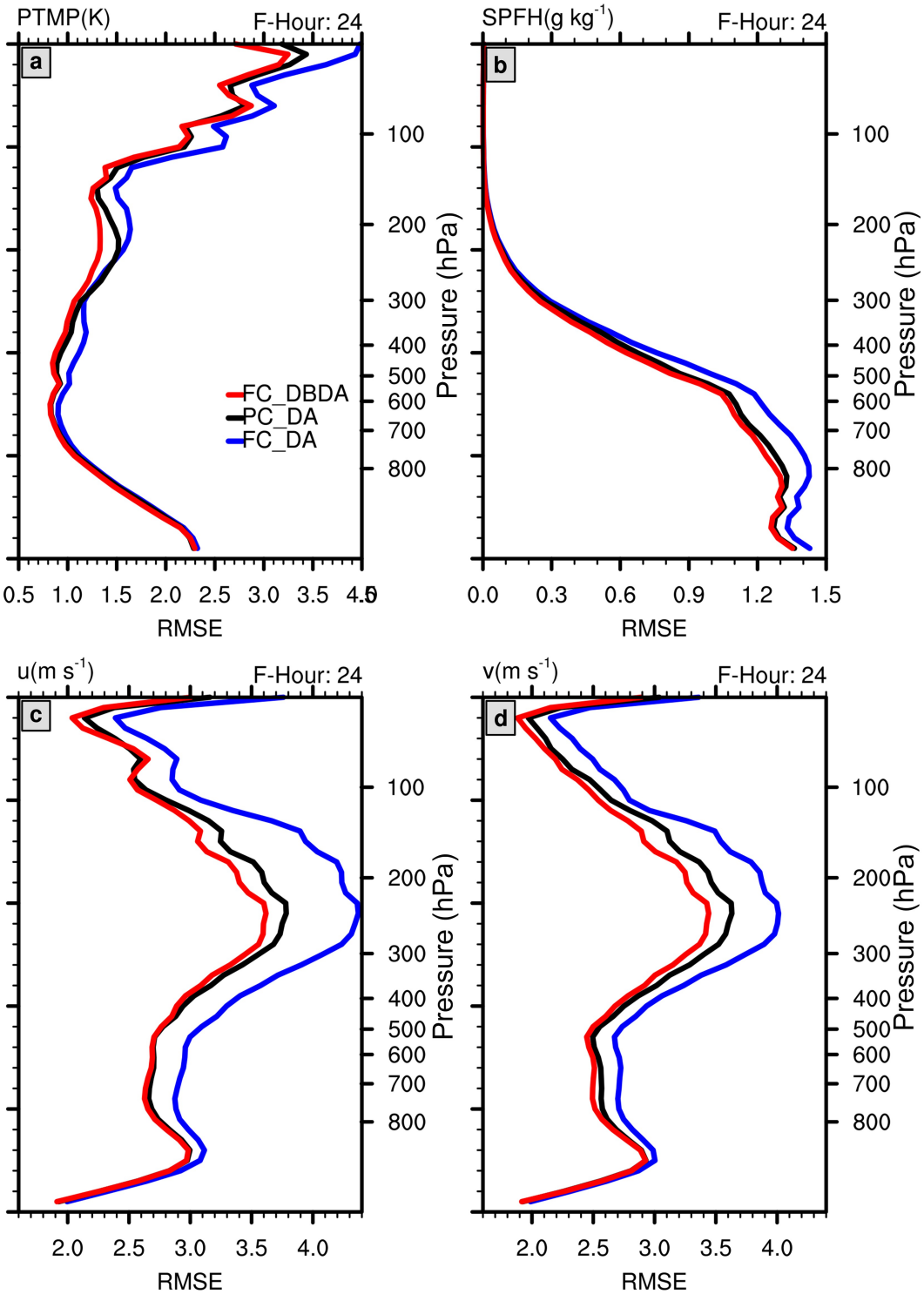

Fig. S8. Same as Fig. S6 but for forecasts at t = 24 h.

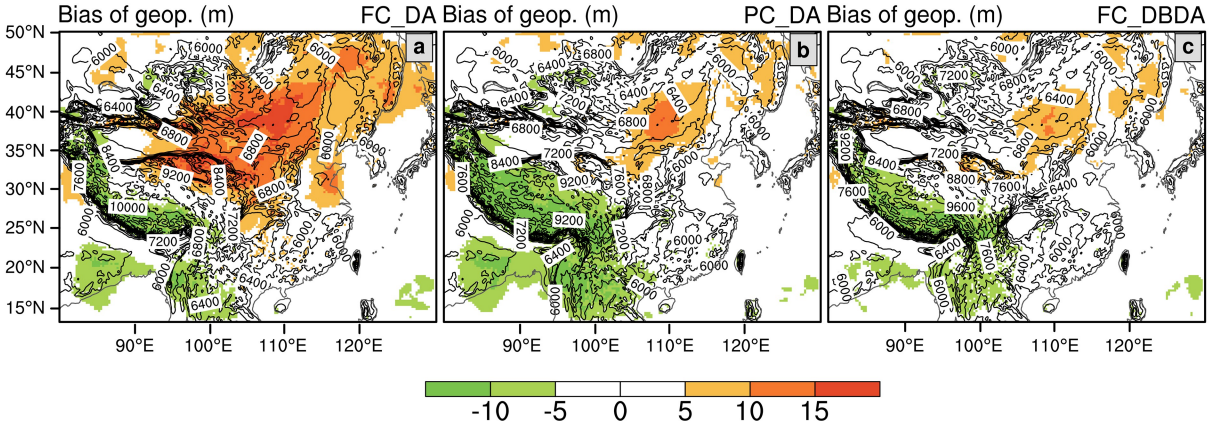

Fig. S9. Geophysical distribution of multicycle-averaged 6-h forecast initial field (contour lines) and bias (shaded) of geopotential height against ERA5 reanalysis data at the 18th model level (~500 hPa) for (a) FC_DA, (b) PC_DA and (c) FC_DBDA respectively.

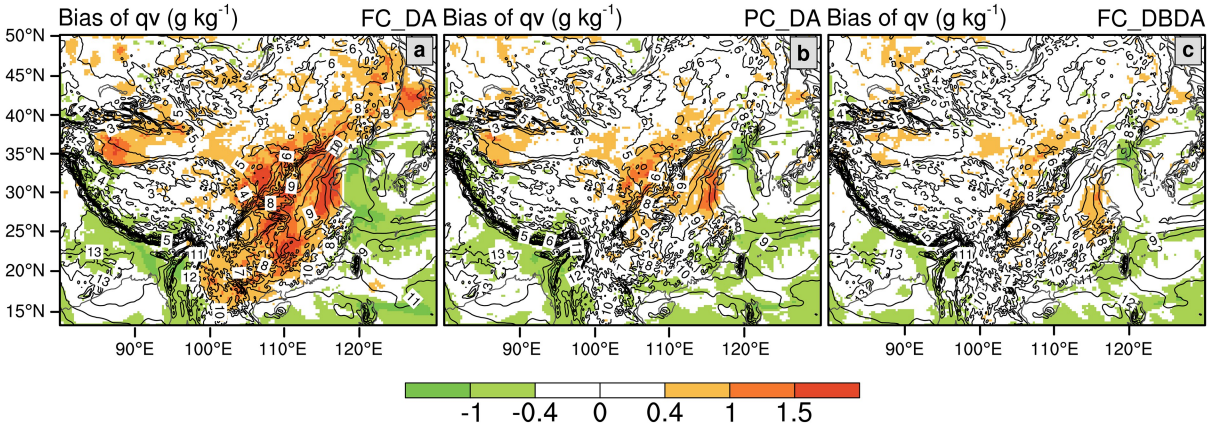

Fig. S10. Same as Fig. S9 but for specific humidity at the 12th model level (~700 hPa).

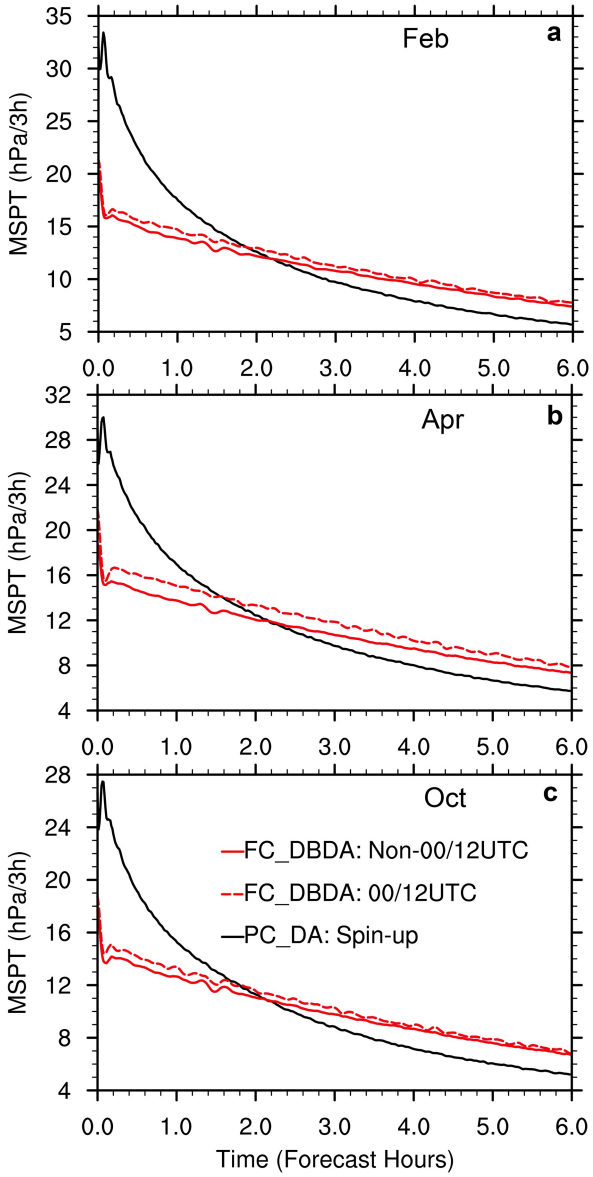

Fig. S11. Multicycle-averaged MSPT during the first 6 forecast hours for February (a), April (b) and October (c) cases. The red (yellow) lines denote the results of the FC_DBDA (spin-up process of PC_DA). The solid (dashed) lines denote the results of cycles that start from non-00/12 UTC (00/12 UTC) cycles of FC_DBDA.

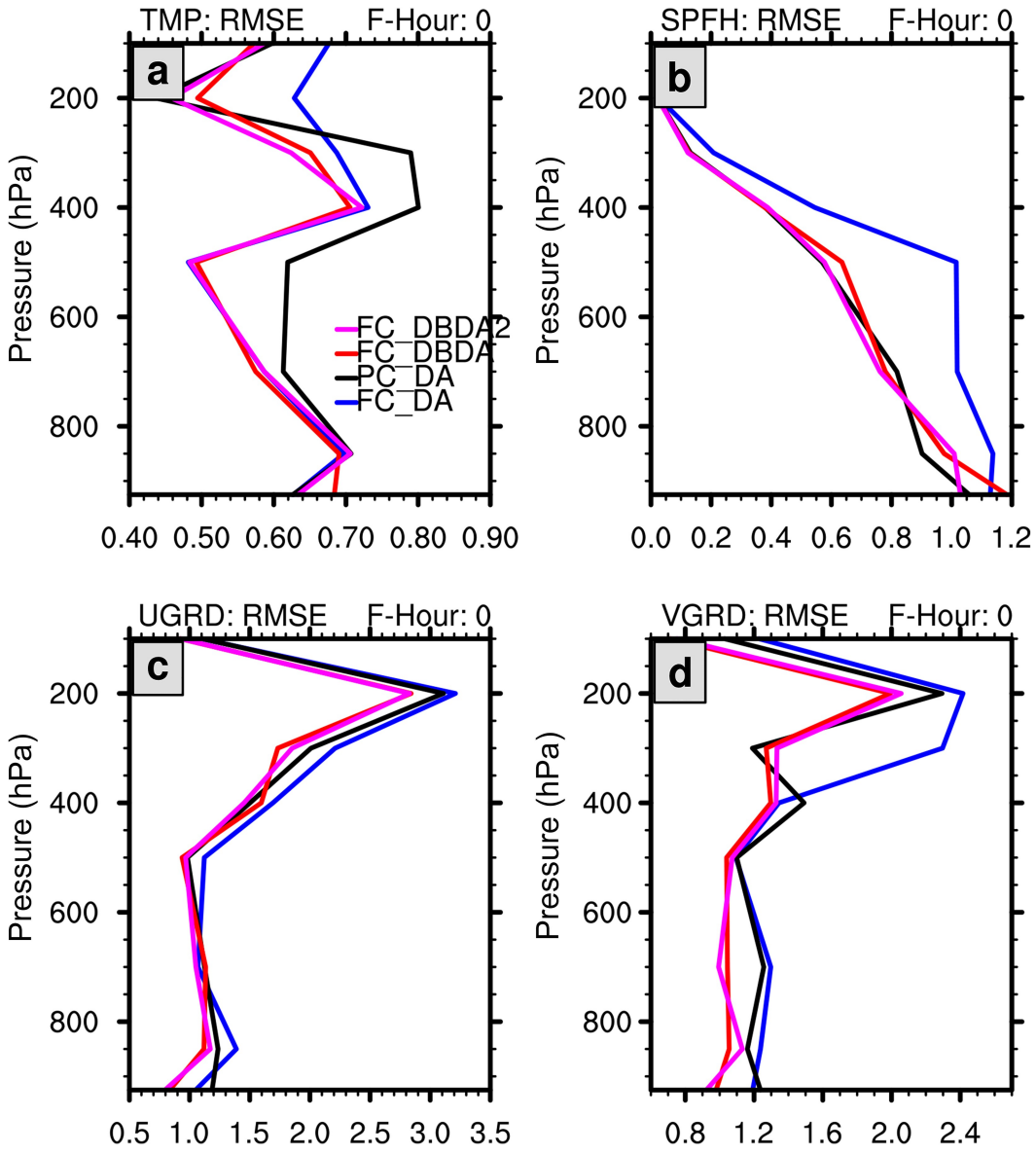

Fig. S12. Same as Fig. 3 but adding the RMSEs of FC_DBDA2 (purple lines).

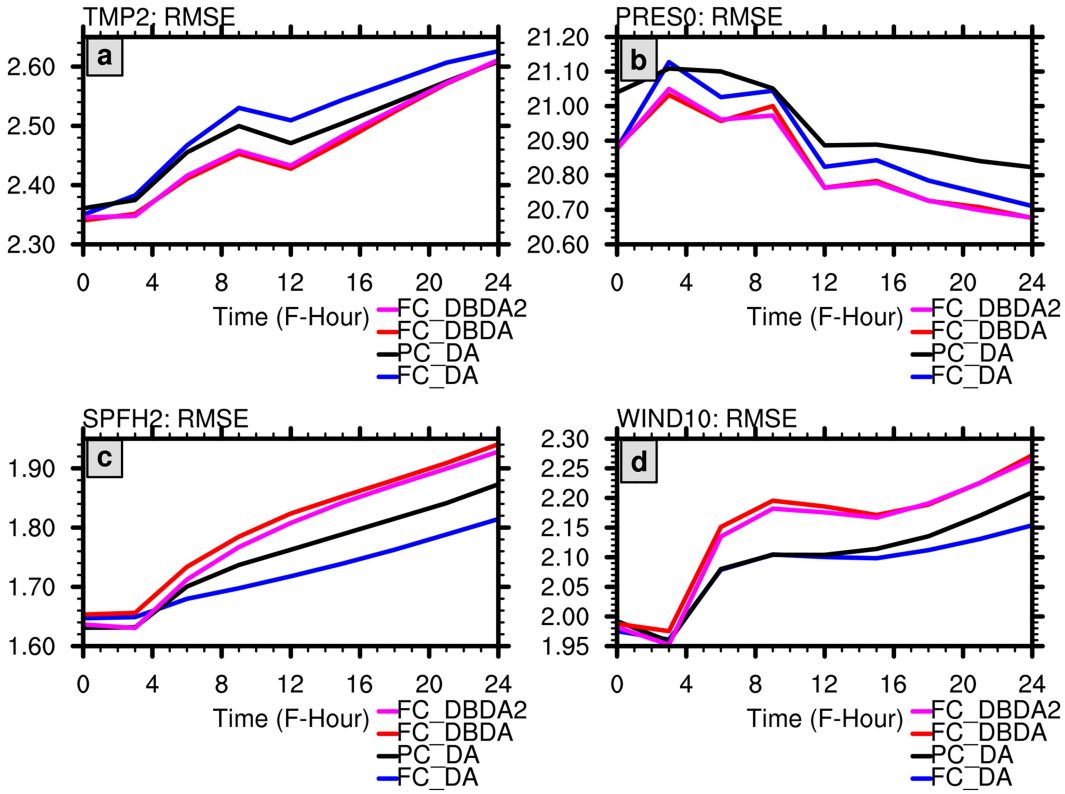

Fig. S13. Same as Fig. 4 but adding the RMSEs of FC_DBDA2 (purple lines).

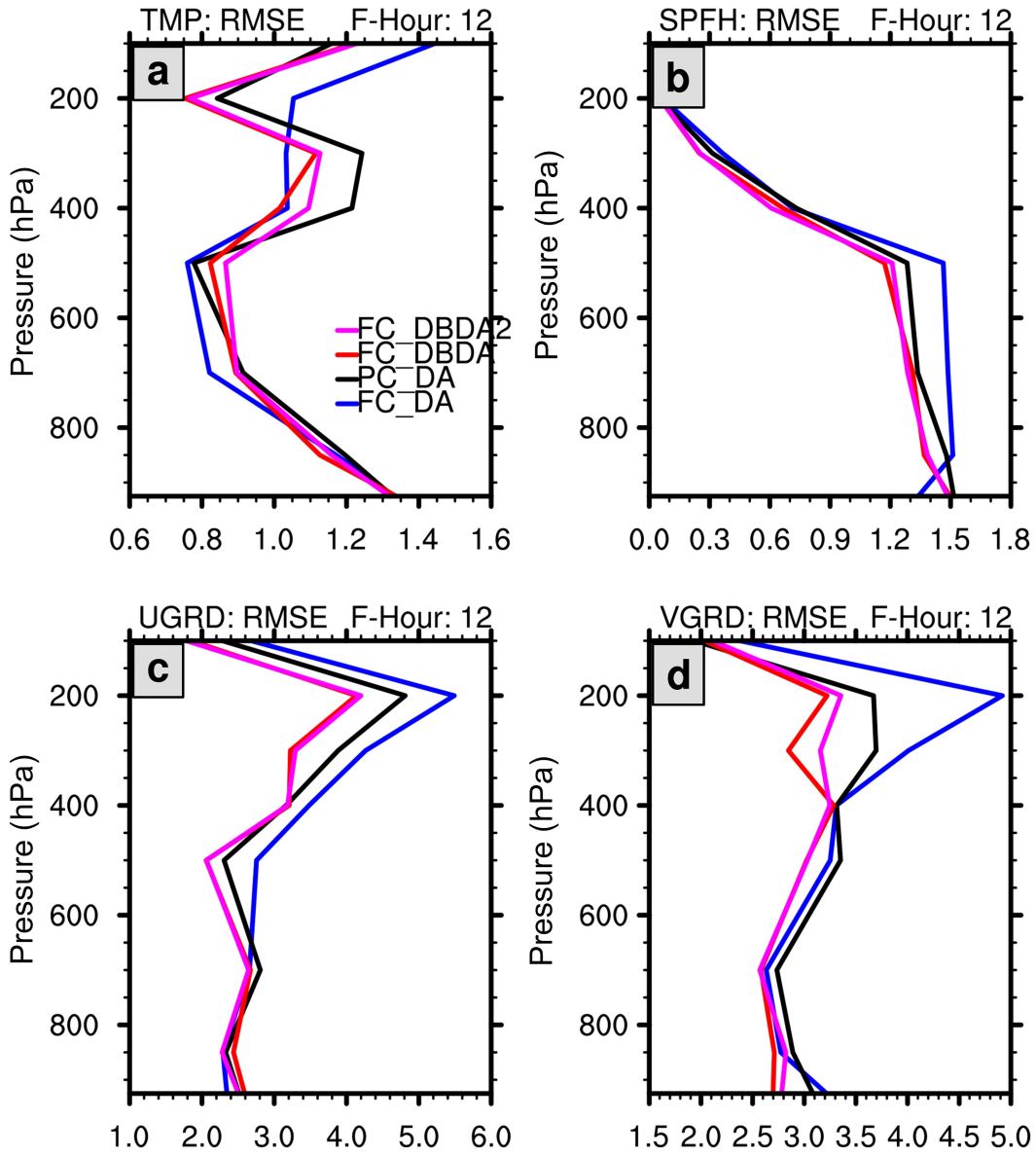

Fig. S14. Same as Fig. S4 but adding the RMSEs of FC_DBDA2 (purple lines).

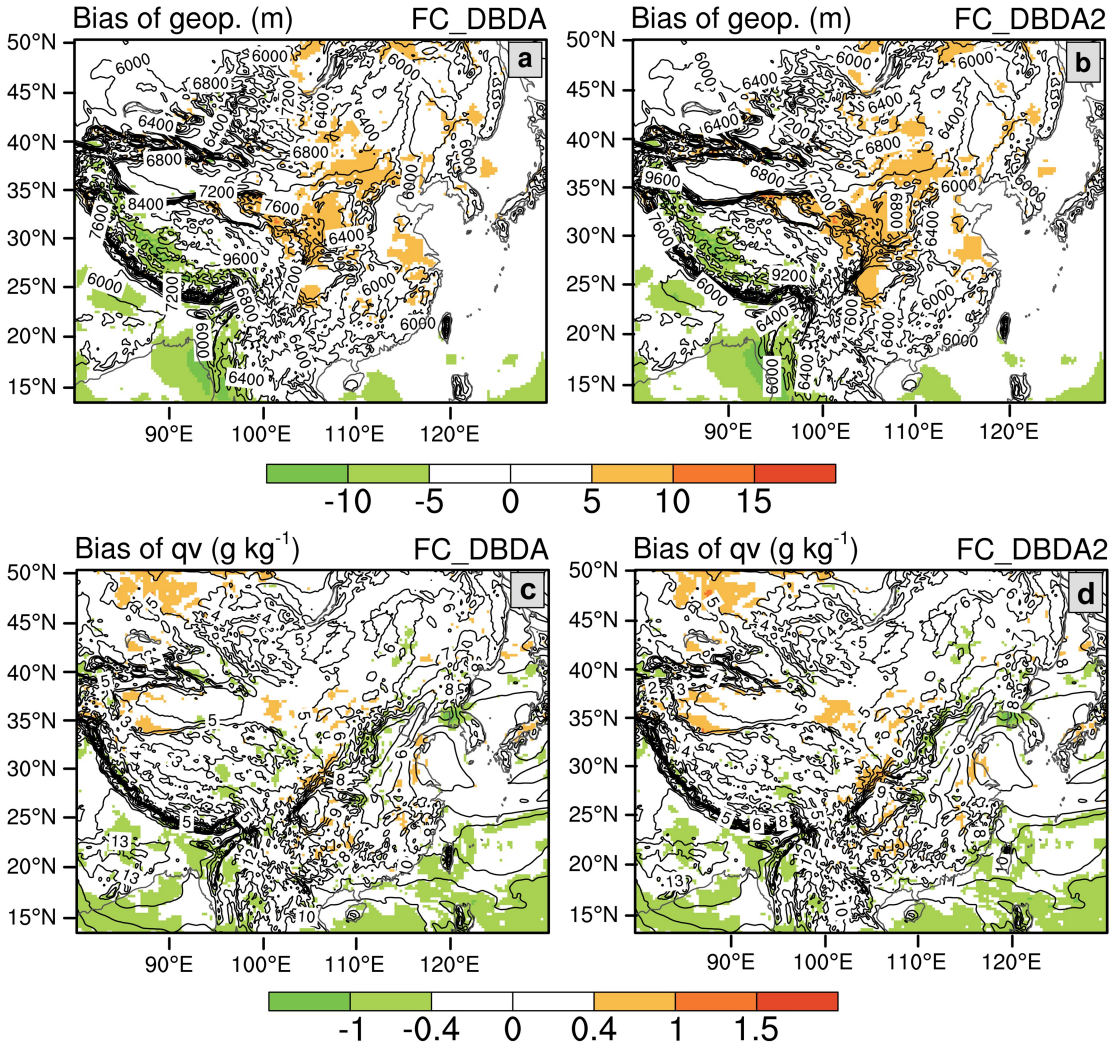

Fig. S15. Same as Fig. 5 but for (a) FC_DBDA and (b) FC_DBDA2.

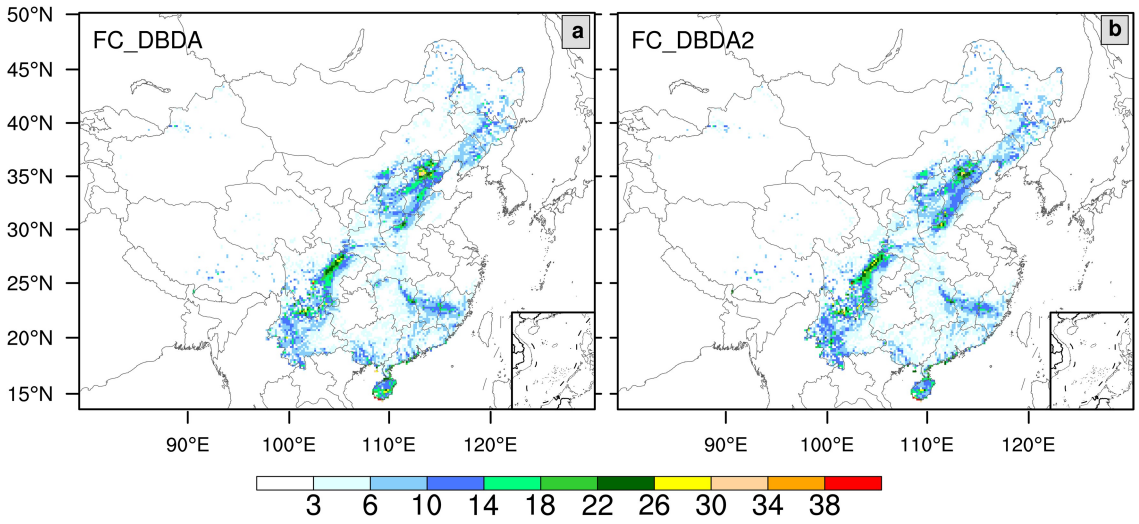

Fig. S16. Same as Fig. 7 but for (a) FC_DBDA and (b) FC_DBDA2.

REFERENCES

Nastrom, G. D., & Gage, K. S., 1985: A Climatology of Atmospheric Wavenumber Spectra of Wind and Temperature Observed by Commercial Aircraft. *Journal of the Atmospheric Sciences*, **42**(9), 950–960, https://doi.org/10.1175/1520-0469(1985)042<0950:ACOAWS>2.0.CO;2.

Lindborg, E., 1999: Can the atmospheric kinetic energy spectrum be explained by two-dimensional turbulence? *Journal of Fluid Mechanics*, **388**, 259–288, https://doi.org/10.1017/S0022112099004851.